Mechanistic Interrogation of Photochemical Nickel-Catalyzed Tetrahydrofuran Arylation Leveraging Enantioinduction Data

Brennan D. McManus, Lang Cheng Hung,[#] Olivia R. Taylor,[#] Paul Q. Nguyen, Alfredo L. Cedeño, Kyle Arriola, Robert D. Bradley, Paul J. Saucedo, Robert J. Hannan, Yvette A. Luna, Phillip Farias, and Ana Bahamonde*

Department of Chemistry, University of California Riverside, Riverside, California, 92521, United States

[#] Contributed equally to this manuscript.

ABSTRACT: This manuscript details the development of an asymmetric variant for the Ni-photoredox α-arylation of tetrahydrofuran (THF), which was originally reported in a racemic fashion by Doyle and Molander. Leveraging the enantioselectivity data that we obtained, a complex mechanistic scenario different from those originally proposed is uncovered. Specifically, an unexpected dependence of the product enantiomeric ratio was observed on both the halide identity (aryl chloride vs. bromide substrates) and the Ni source. Stoichiometric experiments and time course analyses of the evolution of product enantioselectivity with time revealed a different initial behavior for reactions carried out with Ni(II) and Ni(0) pre-catalysts that later converge into a common mechanism. For studying the predominant pathway, this paper describes a rare example of the syntheses of chiral bisoxazoline Ni(II) aryl halide complexes, which proved essential for probing enantioselectivity via stochiometric experiments. These experiments identify the Ni(II) aryl halide complex as the primary species involved in the key THF radical trapping event. A multivariate linear regression model is presented that further validates the dominant mechanism and delineates structure-selectivity relationships between ligand properties and enantioselectivity. EPR analysis of Ni(0)/aryl halide mixtures highlights the fast access to a variety of Ni complexes in 0, +1, and +2 oxidation states that are proposed to be responsible for the initial divergence in mechanism observed when using Ni(0) pre-catalysts. More broadly, beyond advancing the mechanistic understanding of this THF arylation protocol, this work underscores the potential of leveraging enantioselectivity data to unravel intricate mechanistic manifolds within Ni-photoredox catalysis.

INTRODUCTION

Nickel photoredox catalysis is a fast-developing field which has been shown to enable a wide variety of transformations.[1] Contrasting with the fast pace of reaction discovery, mechanistic understanding of these systems has proven more challenging, largely owing to the redox promiscuity of Ni. Indeed, most Ni photoredox protocols are dominated by concurrent side reactions of comproportionation, disproportionation, and photolysis that enable the fast interchange between several oxidation states.[2] In this paper, the identification of a complex mechanistic scenario is described where all of these processes are present and different pathways become more or less prevalent depending on the Ni source and the reaction time.

Specifically, this study focuses on the mechanism of the α-*O*-arylation of tetrahydrofuran (THF), where photolysis of a Ni intermediate was proposed to be responsible for the radical generation that facilitates the C–H abstraction. This mechanistic manifold has been leveraged in other transformations,[3] and was first reported by Doyle and Molander in the context of the THF arylation reaction that we are studying.[3a, 3b] These seminal reports used achiral bipyridine ligands, and we became interested in investigating if this reactivity could also be achieved with a chiral ligand system to render this transformation enantioselective.[4] During our investigations an unexpected dependence of the product enantiomeric ratio (e.r.) on halide identity was observed when switching from aryl chloride to aryl bromide substrates. This data was inconsistent with the previously proposed mechanisms and suggested that the halide atom could be involved in the enantioselectivity-determining step (Figures 1a and 1b).[3a, 3b]

A series of stoichiometric experiments and time course analyses of the reaction enantioselectivity with different Ni sources were then performed. These studies suggested that different mechanisms were favored in the initial reaction stages depending on the Ni source, with these pathways evolving into a common dominant manifold as the reaction progresses. Specifically, a Ni(II) aryl halide intermediate was implicated as the species trapping the carbon-centered radical in most scenarios (Figure 1c). Alternatively, when using (BOX)Ni(COD) as the pre-catalyst, the intermediacy of a different Ni(II) species bearing both aryl and THF ligands was found to prevail at the initial reaction stages (Figure 1d). Notably, $Ni(COD)_2$ was the pre-catalyst used in the seminal aryl chloride report.[3a]

Figure 1. Proposals for the THF radical trapping event

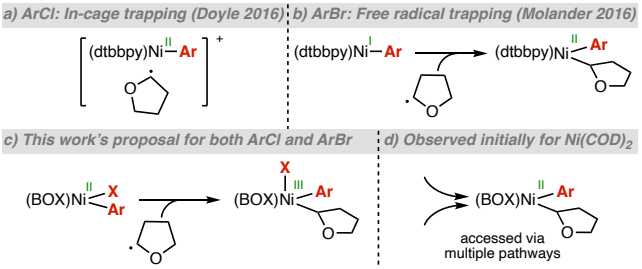

For: dtbbpy = 4,4'-di-*tert*-butyl-2,2'-bipyridyl, Ar = aryl, X = Cl or Br, BOX = bisoxazoline, and COD = 1,5-cyclooctadiene.

It should be noted that, at the onset of our investigations, these mechanistic scenarios had not been proposed (Figures 1c and 1d). However, very recently, the Doyle group published a mechanistic study of this reaction using bipyridine ligands that identified a reaction pathway analogous to that depicted in Figure 1c.[5] Doyle's approach is complementary to the experiments detailed in this manuscript and leverages a series of computations, stoichiometric, and kinetic experiments to elucidate the reaction mechanism. While our analysis largely agrees with Doyle's recent paper, our different approach to investigating this reaction mechanism also allowed us to identify a more intricate scenario where multiple concurrent mechanisms are observed, highlighting both the validity of our approach and its potential to uncover complex mechanistic scenarios.

Beyond the specific findings regarding the mechanism of this reaction, this paper highlights the potential of exploiting enantioselectivity data for mechanistic elucidation. To do so, this paper introduces routes to access a series of chiral bisoxazoline (BOX) Ni(II) aryl halide complexes, which were utilized for key stoichiometric experiments. In contrast to aryl halide oxidative addition bipyridine-ligated Ni complexes, analogous BOX-ligated oxidative addition complexes present a challenging synthesis with limited known examples.[6] Finally, multivariate linear regression (MLR) models are provided that further support the proposed mechanism and identify structure-selectivity relationships between ligand properties and enantioselectivity.

RESULTS AND DISCUSSION

The reaction between THF and methyl 4-chlorobenzoate (**1a**) was chosen as a model system to study the enantioselective α-THF arylation (Table 1). A series of chiral ligands were screened, and it quickly became apparent that BOX ligands outperformed the other chiral ligands tested. A large effect of the oxazoline substituents and methylene bridge substitutions on both yield and enantioselectivity was observed. However, it was unclear based on solely chemical intuition what the optimal substitution at either of these positions might be (entries 1-3). A conventional trial-and-error approach to reaction optimization would require us to synthesize a large number of possible chiral ligand candidates in order to identify those that perform as desired. Instead, to expedite the ligand optimization campaign, MLR models were developed to analyze the results and guide subsequent targeted experimentation.[7] This strategy has been successfully implemented in other Ni-catalyzed enantioselective reaction optimization campaigns.[7a, 7d] An iterative process of ligand synthesis and model refinement eventually converged in the identification of **L4** as the optimal ligand (entry 4, see SI for more details).

Control experiments showed no product formation in the absence of Ni, Ir photocatalyst (PC), or light (entry 5). No reaction was observed for aryl chloride **1a** in the absence of PC when a higher energy wavelength of light was used. However, when using aryl bromide **1b**, these same conditions led to a comparable product yield and better enantioselectivity to those obtained in the photocatalyst-mediated system (entries 6 and 4).[2b, 2f-h, 5, 8] This result will be discussed in detail later in this manuscript. Finally, further optimization of the reaction conditions highlighted that the enantioselectivity could be improved by lowering the temperature, and adding the Ir photocatalyst portion-wise every 12 hours was found to improve the yield (entry 7; please see SI Sections 4-5 and Figure S2 for further details on the reaction optimization and a concise scope exploration, respectively).

Table 1. Reaction optimization

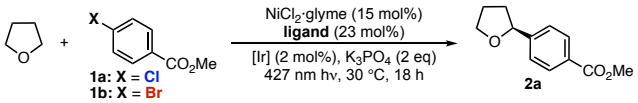

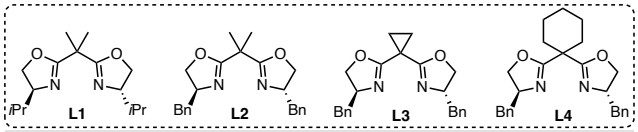

Entry	Ligand	Other variations	ArCl[a]	ArBr[a]
1	**L1**	none	30%, 75:25 e.r.	25%, 61:39 e.r.
2	**L2**	none	40%, 82:18 e.r.	30%, 62:38 e.r.
3	**L3**	none	33%, 80:20 e.r.	25%, 65:35 e.r.
4	**L4**	none	40%, 86:14 e.r.	20%, 57:43 e.r.
5	**L4**	No light, PC, or Ni	n.d.	n.d.
6	**L4**	No PC, 390 nm light	n.d.	32%, 76:24 e.r.
7	**L4**	10 °C	63%, 89:11 e.r.[b]	33%, 79:21 e.r.[c]
8	**L2**	Ni source: $NiBr_2$·glyme	23% 71:29 e.r.	30%, 58:42 e.r.

Reaction conditions: $NiCl_2$·glyme (0.015 mmol), BOX ligand (0.023 mmol), $Ir[dF(CF_3)ppy]_2(dtbbpy)PF_6$ (0.002 mmol), K_3PO_4 (0.2 mmol), aryl chloride **1a** (0.1 mmol) or aryl bromide **1b** (0.1 mmol), and 2 mL of THF, 30 °C. [a] All reported enantiomeric ratios were measured by chiral SFC from the isolated products. All yields were determined by ^1H NMR (n.d. = not detected). [b] Yield of the isolated product after 48 h, with the photocatalyst added portion-wise. [c] $Ir[dF(CF_3)ppy]_2(dtbbpy)PF_6$ (0.0005 mmol), yield of the isolated product after 14 h.

During the optimization campaign, to our surprise, we noticed that drastically different levels of enantioselectivity were obtained using aryl chloride **1a** compared to its bromide analog **1b**. Lower enantioselectivities were consistently obtained for the aryl bromide under a variety of conditions and when using different ligands (Table 1). This halide dependence on e.r. was also observed when switching the pre-catalyst from $NiCl_2$ to $NiBr_2$ (entries 2 and 8). We hypothesized that the lower enantioselectivities observed in the aryl bromide reactions could be due to product racemization or chiral ligand degradation. A time course study of the enantioselectivity was performed for both the aryl chloride and aryl bromide reactions, using $NiCl_2$·glyme and $NiBr_2$·glyme, respectively, to avoid any possible halide scrambling effect. These experiments showed minimal erosion of the enantioselectivity with time for both systems. However, diminished yields were observed at prolonged reaction times only for the aryl bromide system, suggesting that the arylated product is unstable to the aryl bromide reaction conditions. Additional experiments were conducted to study this phenomenon. The isolated **2a** product was added to the coupling of THF with a different aryl bromide. This experiment confirmed the instability of the product to the reaction conditions, but again no changes in the product enantioenrichment were observed (see SI Section 8 for more details). This indicates that neither product racemization nor ligand degradation are likely to be responsible for the e.r. discrepancy.

As shown in Figure 2a, no apparent correlation of the reaction enantioselectivity between the aryl bromide and aryl chloride was observed when using the same BOX ligands. Two mechanistic hypotheses can explain these results:

(1) The aryl chloride and bromide reactions may undergo different mechanisms.

(2) Both reactions follow analogous mechanisms, but a halogen atom is bound to Ni when the carbon-centered radical is trapped.

To challenge the possibility of a common mechanism for both aryl halides, we tested if the enantioselectivities obtained for **1a** and **1b** substrates, while disparate, could be statistically modeled together. Our hypothesis was that if a correlation can be found between e.r. and the properties of the common reaction intermediate that traps the carbon-centered radical, this would support a common mechanism. Specifically, it was hypothesized that the Ni(II) aryl halide complex could be the species that traps the THF radical, and that the divergent properties of the chloride and bromide adducts may be responsible for the divergent enantioselectivities. Additionally, this Ni(II) complex would be expected to be more stable than other Ni(I) or Ni(0) complexes, and therefore it would be present in higher concentration in solution and be more likely to trap a free THF radical.

To initiate statistical modeling, the properties of (BOX)Ni phenyl chlorides and bromides bearing the ligands utilized in this study were calculated. Specifically, gas-phase conformational searches (OPLS4,[9] MacroModel[10]) gave representative ensembles of energetically accessible conformers (<5 kcal/mol). These low energy Ni conformers were subjected to DFT geometry optimization (B3LYP-D3BJ/6-31G**-lanl2dz[Ni]), followed by single-point calculations to obtain energies and properties (M06-D3/def2tzvp-SDD[Ni]-SMD[THF]).[11]

A forward stepwise algorithm was used to identify MLR models that would capture both aryl chloride and aryl bromide enantioselectivity trends.[7] As shown in Figure 2b, a statistically robust model was found that correlates the measured enantioselectivities with computed properties of the (BOX)Ni aryl halide complexes. The validity of the model is highlighted by its high leave-one-out (LOO) Q^2 value and the training mean absolute error (MAE). Notably, despite the large amount of withheld data (40% test:training split),[12] excellent predictions for the test set were also obtained as indicated by the test R^2 and MAE values. The model robustness was independent of the test/training splitting algorithm used (see SI for more details).

This model includes two parameters related to the three-dimensional structure of the complex, each describing angles within the oxazoline cores. These descriptors capture the asymmetry of the complex, with α describing the oxazoline *trans* to the halogen and β referring to the oxazoline *trans* to the phenyl group. Another parameter describes the difference in the spatial accessibility to the Ni center from each face, as quantified using the recently reported AtomAccess descriptor (accessibility ratio, orange box).[13] Specifically, this parameter measures the percentage of the unblocked paths to Ni on the less accessible face. A higher accessibility ratio (closer to 50%) indicates that access to Ni from either face is relatively similar. The negative coefficient for this parameter in the model indicates that Ni complexes where one face is blocked, which are therefore more likely to trap the THF radical only on the most accessible face, are predicted to provide higher enantiocontrol.

Additionally, the model contains a descriptor of the phenyl ring distortion, measuring the average angle among the carbons of the aromatic system (γ; similar correlations were also found with the average C–C distances). Notably, this is the only parameter in the model that separates the bromide from the chloride complexes. The chloride complexes present little to no distortion of the aromatic ring, with average angles close to the ideal 120° for all complexes. In contrast, the bromide complexes present a wider range of γ angles.

We hypothesized that the arene distortion could arise from either: (1) a non-covalent interaction (NCI) involving the arene; or (2) changes in the Ni–arene bonding that are indirectly dependent on the halogen. Hypothesis 2 was discarded, as no correlation was observed between γ and any Ni electronic descriptors. Among possible NCIs, we initially considered a direct interaction between the bromide and the arene; however, γ is not correlated with either the bromide-arene distance or with any bromide electronic descriptors. We then extended our search for other parameters that correlated with γ and identified a correlation with the calculated NMR shift at H^a ($R^2 = 0.73$). This suggests that the arene distortion may be a reporter for a C–H-π interaction between the arene and H^a. Finally, no such correlation was observed in the chloride series, suggesting this non-covalent interaction is specific to the Ni(II) aryl bromides (see SI for further details).

Figure 2. Enantioselectivity changes and MLR model for aryl chlorides vs aryl bromides

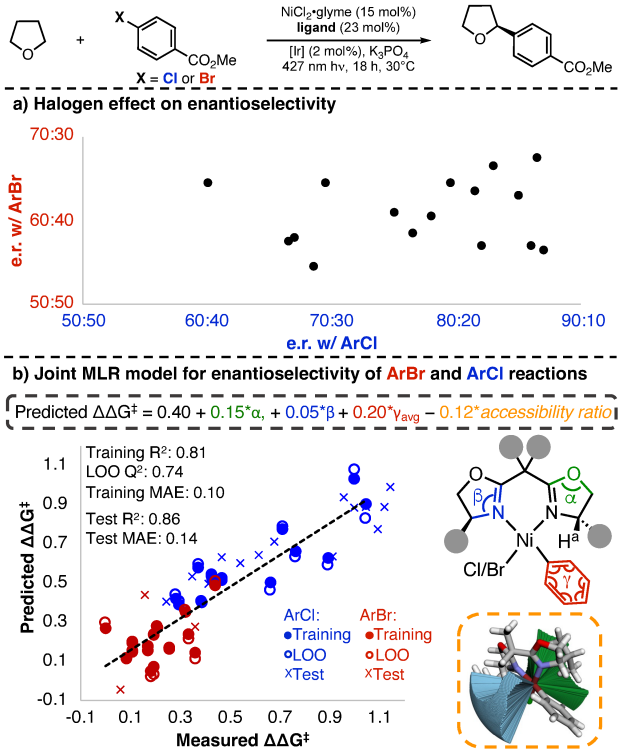

a) Comparison of the enantioselectivities obtained for **1a** *vs* **1b** utilizing the same ligand. b) MLR model expressing the enantioselectivities obtained for **1a** and **1b** in terms of properties of the (BOX)Ni aryl halide complexes hypothesized to be involved in product formation. 40% test:training split with Kennard-Stone algorithm.[12] All reported values are enantiomeric ratios measured by chiral SFC from the isolated products. The accessibility ratio image was generated with Chilton's web tool ref. 13b, initially reported in ref. 13a. Copyright 2023 American Chemical Society.

Other steric and electronic descriptors that differentiate chloride and bromide complexes were also identified. However, they do not

appear in the model because they do not show as strong of a correlation with the enantioinduction as γ. Nonetheless, these descriptors highlight the electronic and conformational changes triggered by the identity of the halogen, which are believed to collectively account for the significant difference in enantioinduction observed. A detailed analysis considering these descriptors is provided in the SI.

To challenge the mechanistic relevance of the (BOX)Ni aryl halide correlation depicted in Figure 2b, we then tested if models could also be constructed from other halide-bonded Ni complexes. The properties of (BOX)Ni dihalide complexes were calculated and these molecular descriptors were subjected to the modeling workflow previously described. The models obtained presented worse statistics and failed to validate over different data splits, which is characteristic of overfitting (see SI for further details). This further supports the involvement of the (BOX)Ni aryl halide complexes in the enantioselectivity-determining step of the reaction.

Intrigued by this preliminary result suggesting that the Ni(II) oxidative addition complex may be trapping the THF radical (Figure 1c), we decided to further investigate this mechanistic manifold. We first aimed to conduct stoichiometric experiments where the THF radical is generated independently in the presence of different Ni(II) aryl halide BOX complexes.[14] The objective of these experiments is to compare the enantioselectivity data obtained from stoichiometric and catalytic experiments to further probe the possible involvement of the Ni(II) oxidative addition complex in the enantioselectivity-determining step. If the enantioselectivity values obtained under the stoichiometric conditions are in accordance with those measured under the catalytic conditions, this would strongly suggest that this is the Ni complex that traps the radical species. Furthermore, this approach would allow us to study both the aryl chloride and aryl bromide reactions separately and challenge the common mechanism hypothesis.

The synthesis of a series of aryl bromide and aryl chloride (BOX)Ni(II) complexes was more challenging than expected. Contrasting with the numerous syntheses of achiral Ni(II) oxidative addition complexes, chiral variants are more limited.[14-15] This is especially true for BOX ligands, despite being one of the most commonly used chiral ligand scaffolds in Ni catalysis. To our knowledge, only one Ni alkyl bromide and two aryl bromide oxidative addition complexes have been reported, and the synthesis of BOX-Ni aryl chloride complexes was unknown.[6, 16]

Based on the reported (BOX)NiPhBr complex synthesis, we envisioned accessing the desired Ni(II) complexes via Ni(0) oxidative addition into the aryl halide (Figure 3).[6] Instead of the optimal **L4**, **L2** was utilized as ligand because it works comparably to **L4** and it is commercially available. The use of pentane as the solvent was found to be key for obtaining the (BOX)Ni(COD) adduct (**I**), as this enabled separation of free 1,5-cyclooctadiene (COD) by filtration.[6, 16] At this stage, previously reported procedures proceeded without any further purification. However, when we aimed to telescope this crude mixture by exposing it to aryl halides, the desired Ni(II) complexes were obtained in low yields and our attempts to purify them were intractable. It was found that a subsequent ether wash could be used to separate the desired Ni(0) precursor **I** from any remaining unreacted $Ni(COD)_2$ (see SI for details). This purified Ni(0) complex then allowed us to synthesize a series of Ni aryl bromides (**II-Br**) and aryl chlorides (**II-Cl**) via oxidative addition at room temperature under a large excess of the aryl halides.

The Ni aryl bromide complexes were accessible in ether, and both a complex bearing an *ortho*-substituted arene (**II-Br2**) and the model substrate **1b** (**II-Br1**) were obtained. The structure of **II-Br2** was unambiguously established by X-Ray single crystal diffraction, revealing a distorted square planar geometry (Figure S23). The slower oxidative addition of the aryl chloride prevented us from isolating the Ni(II) complex for the model substrate due to competitive biaryl formation. However, *ortho*-substituted arenes, which reduced the bimolecular transmetallation processes that lead to biaryl formation, were amenable to this synthetic pathway (**II-Cl1** and **II-Cl2**).

Figure 3. Synthesis of (BOX)Ni aryl halide complexes

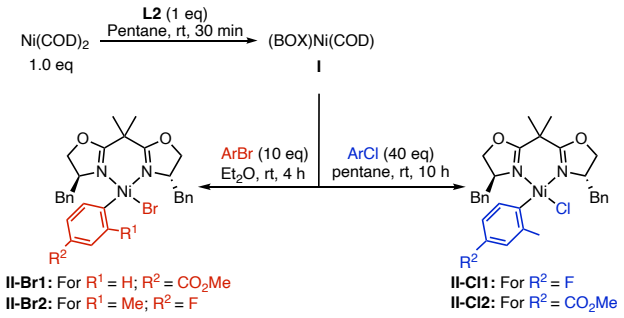

With the complexes in hand, we then needed to identify conditions where the THF radical can be generated and the Ni(II)complexes are stable. To reduce complications from possible energy transfer pathways, approaches that require photocatalysts were avoided. Di-*tert*-butyl peroxide had been reported to facilitate the formation of the THF radical under thermal conditions for a Ni-catalyzed cross-electrophile coupling reaction.[17] Dual activation of the peroxide by moderate heating and blue light irradiation allowed us to promote the THF radical formation at 30 °C. Under these conditions no product formation was observed in the absence of the peroxide.

Table 2. Enantioselectivity comparison for stoichiometric and catalytic experiments

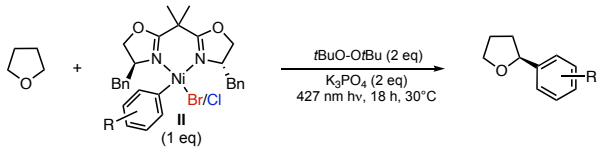

Entry	Aryl halide	Catalytic data	Stoichiometric data
1	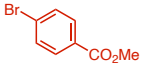	62:38 e.r. (30% yield)	62.5:37.5 e.r. (47% yield)
2	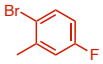	64.5:35.5 e.r. (16% yield)	63.5:36.5 e.r. (60% yield)
3	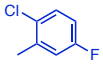	80.5:19.5 e.r. (4% yield)	81.5:18.5 e.r. (17% yield)
4	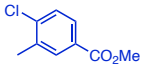	84:16 e.r. (21% yield)	84:16 e.r. (56% yield)

Stoichiometric reaction conditions: (**L2**)NiArX (0.05 mmol), (t-BuO)$_2$ (0.1 mmol), K_3PO_4 (0.2 mmol), and 2 mL of THF, 30 °C. Catalytic reaction conditions (Figure 2): $NiCl_2$·glyme (0.01 mmol), BOX ligand (0.015 mmol), Ir[dF(CF_3)ppy]$_2$(dtbbpy)PF_6 (0.002 mmol), K_3PO_4 (0.2 mmol), aryl chloride **1a** (0.1 mmol) or aryl bromide **1b** (0.1 mmol), and 2 mL of THF, 30 °C. All reported enantiomeric ratios were measured by chiral SFC from the isolated products.

As shown in Table 2, the enantiomeric ratios obtained for stoichiometric and catalytic reactions were all nearly identical, thus strongly suggesting that Ni(II) complex **II** is the species that traps the THF carbon-centered radical. Furthermore, these stoichiometric experiments led to product formation in higher yields than the catalytic conditions, consistent with the slow rates of oxidative addition for *ortho*-substituted aryl halides.

Figure 4. Crossover experiments with Ni complex II as Ni source

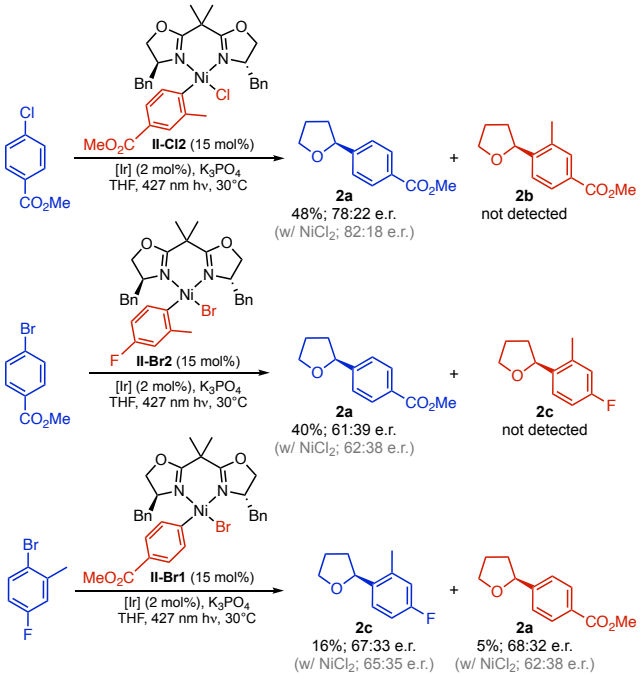

Reaction conditions: (**L2**)Ni(ArX) **II** (0.01 mmol), Ir[dF(CF$_3$)ppy]$_2$(dtbbpy)PF$_6$ (0.002 mmol), K$_3$PO$_4$ (0.2 mmol), aryl chloride or aryl bromide **1b** (0.1 mmol), and 2 mL of THF, 30 °C. NiCl$_2$ reaction conditions (Figure 2): NiCl$_2$·glyme (0.01 mmol), BOX ligand **L2** (0.015 mmol), Ir[dF(CF$_3$)ppy]$_2$(dtbbpy)PF$_6$ (0.002 mmol), K$_3$PO$_4$ (0.2 mmol), aryl chloride (0.1 mmol) or aryl bromide (0.1 mmol), and 2 mL of THF, 30 °C. All reported enantiomeric ratios were measured by chiral SFC from the isolated products, and yields were calculated via NMR of the crude reaction mixtures.

We then tested if these Ni(II) complexes could be used as pre-catalysts for the reaction. Specifically, crossover experiments where the aryl halide in solution was different from the aryl halide within **II** were conducted, so as to have an enantioselectivity handle for both initial and subsequent catalytic turnover (Figure 4). When using **II-Cl2** or **II-Br2** as the Ni source, no product bearing the *ortho*-substitution was observed, and **2a** was obtained as sole THF arylation product. This outcome was also observed by Doyle when studying this reaction with 4,4'-di-*tert*-butyl-2,2'-bipyridine (dtbbpy) as ligand.[5] They demonstrated that under these conditions photochemically-induced reductive elimination of **II** gives access to Ni(0) complexes. This allows for the swapping of the aryl groups within **II,** where the faster reactivity of the less sterically hindered **1a** explains why **2a** is observed as the product. Finally, when **II-Br1** was used as the pre-catalyst, both products were observed.

While the product distribution is not unprecedented,[5] the enantioselectivity readout is unique to our approach and allows us to further probe the pathway(s) accessed under these conditions. Specifically, comparison of the product enantioselectivities obtained in these crossover experiments with those obtained using different Ni sources allows us to identify if the same mechanisms are operative.

The analysis of the enantioselectivities obtained utilizing these Ni(II) complexes as Ni sources revealed an intriguing behavior (Figure 4). The asymmetric induction analysis of **2a** reveals lower enantioselectivity when using **II-Cl2** (78:22 e.r.) instead of NiCl$_2$ (82:18 e.r.) as the pre-catalyst. On the other hand, the aryl bromide reactions produced the product bearing the arene of the added substrate in similar enantioselectivity (products depicted in blue). Interestingly, higher stereo-control was observed when **II-Br1** was used as the Ni source to yield **2a** (red product, 68:32 e.r. with **II-Br1** vs 62:38 with NiCl$_2$).

The different enantioselectivities observed when utilizing NiCl$_2$ or Ni(II) complex **II** as the Ni source suggest that different pathways can be accessed under these conditions. Given that these Ni(II) oxidative addition complexes should be readily accessed in the presence of Ni(0), we wondered how the product enantioselectivity would compare when using Ni(COD)$_2$ as the pre-catalyst.

The direct use of Ni(COD)$_2$ as the pre-catalyst leads to no product formation. However, preformed (BOX)Ni(COD) **I** was found to be a suitable pre-catalyst. In all four cases studied, a different enantioselectivity was observed for reactions performed with these two Ni sources (Table 3). Switching from the Ni(II) source to using this Ni(0) source resulted in lower enantioselectivities for aryl chloride substrate **1a** and higher enantioselectivities for aryl bromide **1b**. While some of these changes were substantial (5-10% e.r., entries 2 and 4), even seemingly more subtle changes (entries 1 and 3) did not show any variation upon conducting the experiments in duplicate.

Table 3. Enantioselectivity comparison for different Ni sources

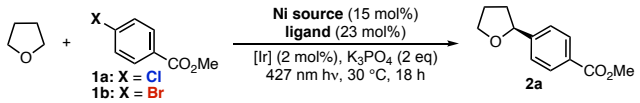

Entry	Aryl halide, ligand	NiCl$_2$•glyme	(BOX)Ni(COD)
1	**1a**, **L2**	82:18 e.r. (40% yield)	80:20 e.r. (55% yield)
2	**1a**, **L4**	86:14 e.r. (40% yield)	81:19 e.r. (3% yield)
3	**1b**, **L2**	62:38 e.r. (30% yield)	64:36 e.r. (31% yield)
4	**1b**, **L4**	57:43 e.r. (20% yield)	67:33 e.r. (10% yield)

NiCl$_2$ reaction conditions: NiCl$_2$·glyme (0.015 mmol), BOX ligand (0.023 mmol), Ir[dF(CF$_3$)ppy]$_2$(dtbbpy)PF$_6$ (0.002 mmol), K$_3$PO$_4$ (0.2 mmol), aryl chloride **1a** (0.1 mmol) or aryl bromide **1b** (0.1 mmol), and 2 mL of THF, 30 °C. (BOX)Ni(COD) reaction conditions: (BOX)Ni(COD) **I** (0.015 mmol), Ir[dF(CF$_3$)ppy]$_2$(dtbbpy)PF$_6$ (0.002 mmol), K$_3$PO$_4$ (0.2 mmol), aryl chloride **1a** (0.1 mmol) or aryl bromide **1b** (0.1 mmol), and 2 mL of THF, 30 °C. All reported enantiomeric ratios were measured by chiral SFC from the isolated products, and yields were calculated via ^{1}H NMR of the crude reaction mixtures.

Intrigued by this modest but consistent enantioselectivity dependence on Ni pre-catalyst, and given that Ni(COD)$_2$ was the Ni source utilized in the seminal report for the aryl chloride THF arylation,[3a] we decided to further investigate this behavior. While this data alone cannot definitely discard different Ni pre-catalysts operating via distinct pathways, we reasoned that a more likely scenario would be an initial divergence that evolves into a common dominant mechanism for all pre-catalysts. We envisioned that this hypothesis could be tested by analyzing the product enantioselectivities at early reaction time points.

Figure 5. Enantioselectivity evolution through time for different Ni pre-catalysts

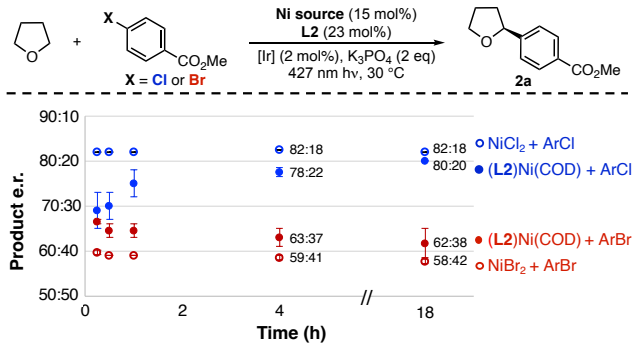

$NiCl_2$ reaction conditions: $NiCl_2$·glyme (0.030 mmol), BOX ligand **L2** (0.046 mmol), Ir[dF(CF_3)ppy]$_2$(dtbbpy)PF_6 (0.004 mmol), K_3PO_4 (0.4 mmol), aryl chloride **1a** (0.2 mmol), and 4 mL of THF, 30 °C. $NiBr_2$ reaction conditions: $NiBr_2$·glyme (0.030 mmol), BOX ligand **L2** (0.046 mmol), Ir[dF(CF_3)ppy]$_2$(dtbbpy)PF_6 (0.004 mmol), K_3PO_4 (0.4 mmol), aryl bromide **1b** (0.2 mmol), and 4 mL of THF, 30 °C. (**L2**)Ni(COD) conditions: (**L2**)Ni(COD) **I** (0.030 mmol), Ir[dF(CF_3)ppy]$_2$(dtbbpy)PF_6 (0.004 mmol), K_3PO_4 (0.4 mmol), aryl chloride **1a** (0.2 mmol), and 4 mL of THF, 30 °C. All reported enantiomeric ratios were measured by chiral SFC from the isolated products. The error bars represent the standard deviation in e.r. for each data point from duplicate experiments.

Figure 5 show the time-course of product enantioselectivities obtained for the model aryl chloride **1a** utilizing either $NiCl_2$·glyme or (**L2**)Ni(COD) **I** as Ni sources. The $NiCl_2$ reaction shows a steady enantioselectivity (82:18 e.r.) that is highly reproducible though different runs. In sharp contrast, the (**L2**)Ni(COD) **I** reaction displays a reproducible enantioselectivity evolution from a lower enantiocontrol regime that asymptotes towards the enantioselectivity observed for the $NiCl_2$ reaction. Negligible variations in the product enantioselectivities were observed between the 4-hour time point and the overnight reactions depicted in Table 3. Finally, a control reaction adding 15 mol% COD to the $NiCl_2$·glyme reaction was carried out to discard a possible influence of the diene on enantioinduction, and no effect on product enantioselectivity was observed.

We then tried to extend these experiments to the aryl bromide chemistry. The use of $NiCl_2$ with aryl bromide **1b** yields a higher initial enantioselectivity (77:23 e.r. after 15 min) that quickly evolves into a steady 62:38 e.r. (see SI, Figure S3). This behavior is probably associated with the initial competition of chloride and bromide halogens as Ni ligands. Furthermore, the stability of the e.r. from 4 h onwards is at odds with the ligand degradation hypothesis for the lower e.r. for aryl bromides relative to aryl chlorides, as a constant decrease in enantioselectivity would have been expected in that case.

To avoid complications related to the presence of multiple halides at the beginning of the reaction, $NiBr_2$·glyme was tested as the pre-catalyst. As shown in Figure 5, a steady product enantioselectivity was observed when using $NiBr_2$·glyme in conjunction with aryl bromide **1b**, with minimal enantioselectivity erosion observed over time. The time course of the (**L2**)Ni(COD)-mediated reaction with **1b** again showed a different behavior from that obtained for the Ni(II) system. In this case, the enantioselectivity obtained initially is similar to the (**L2**)Ni(COD) aryl chloride system and later evolves asymptotically towards the lower values observed when using $NiBr_2$·glyme.

These results suggest the presence of a competing pathway that is more relevant when Ni(0) complex **I** is in higher concentration. The asymptotic evolution of the enantioselectivity through time suggests a switch to a different predominant mechanism as the reaction proceeds, which can otherwise be directly accessed when utilizing $NiCl_2$ as the pre-catalyst. The stoichiometric experiments (Table 2) and MLR modeling (Figure 2b) presented earlier strongly support that THF radical trapping by Ni(II) complex **II** is the predominant mechanism as the reaction progresses. We reasoned that the initial behavior observed with Ni(0) pre-catalysts could be rationalized by free radical trapping by other Ni species that are quickly formed and are prevalent at early time points. When compared to the Ni(II)-initiated reactions, Ni(0)-initiated reactions consistently show less divergent enantioselectivity values between aryl chloride and bromide reactions (Table 3). These effects, together with the matching enantioselectivity at early time-points for both halide systems (Figure 5), suggests that the mechanism accessed utilizing Ni(0) pre-catalysts is agnostic of the halogen.

The direct trapping of the THF radical by Ni(0) complex **I**, which can lead to product formation via oxidative addition into the aryl halide and subsequent reductive elimination (Pathway A, Figure 6b), would be the simplest explanation for this data.[18] However, we decided to further investigate if other Ni species could be formed sufficiently quickly and have lower activation barriers to product formation to account for this initial behavior.

Fast comproportionation and disproportionation events for Ni complexes are well established.[2] Thus, we wondered if these processes would be fast enough to be relevant to the initial divergent pathway observed for the Ni(0) THF arylation chemistry. To test this hypothesis, a series of EPR measurements were performed using the ubiquitous dtbbpy ligand for facilitating more straightforward comparisons with the literature values.[2, 8c] We started our investigation by mixing a THF solution of dtbbpy and Ni(COD)$_2$ with another THF solution containing aryl chloride **1a**. Both solutions were injected at the same time directly in the EPR tube. The resulting mixture was subsequently frozen with liquid N_2 after 10 seconds (no light irradiation nor photocatalyst were included in this experiment). A strong EPR signal characteristic of Ni(I) formation was observed (Figure 6a).[2, 8c] We then repeated the same procedure for aryl bromide **1b**, and a Ni(I) signal was again obtained (see SI, Figure S8). This experiment was repeated with 1-bromo-4-fluoro-2-methylbenzene and 1-chloro-4-fluoro-2-methylbenzene to reduce the rate of oxidative addition and biaryl formation. Under these conditions, the formation of Ni(I) complexes was also observed (see SI, Figures S9 and S10). Finally, for comparison, additional spectra mixing the same dtbbpy/Ni(COD)$_2$ solution with solutions of dtbbpy and

$NiCl_2$·glyme or $NiBr_2$·glyme and the isolated 1-bromo-4-fluoro-2-methylbenzene (dtbbpy)Ni aryl bromide oxidative addition complex[2a] were measured (see SI, Figures S5-S6, and S10). These controls are known to readily yield Ni(I) halide complexes. The same general features characteristic of Ni(I) species were observed in all of the spectra, with subtle differences arising for the different arenes and halides used (see SI for details).

When mixing a Ni(0) source with aryl halides, oxidative addition will readily occur to yield Ni(II) complex **II** (Figure 6b). Complexes **I** and **II** are not EPR active and cannot account for the observed signals, which are characteristic of Ni(I) complexes. The formation of the Ni(I) complexes observed by EPR is proposed to arise from a comproportionation between **I** and **II**, which would yield intermediates **III** and **IV** (see blue arrows in Figure 6b).

Figure 6. Alternative accessible pathways at higher Ni(0) concentrations

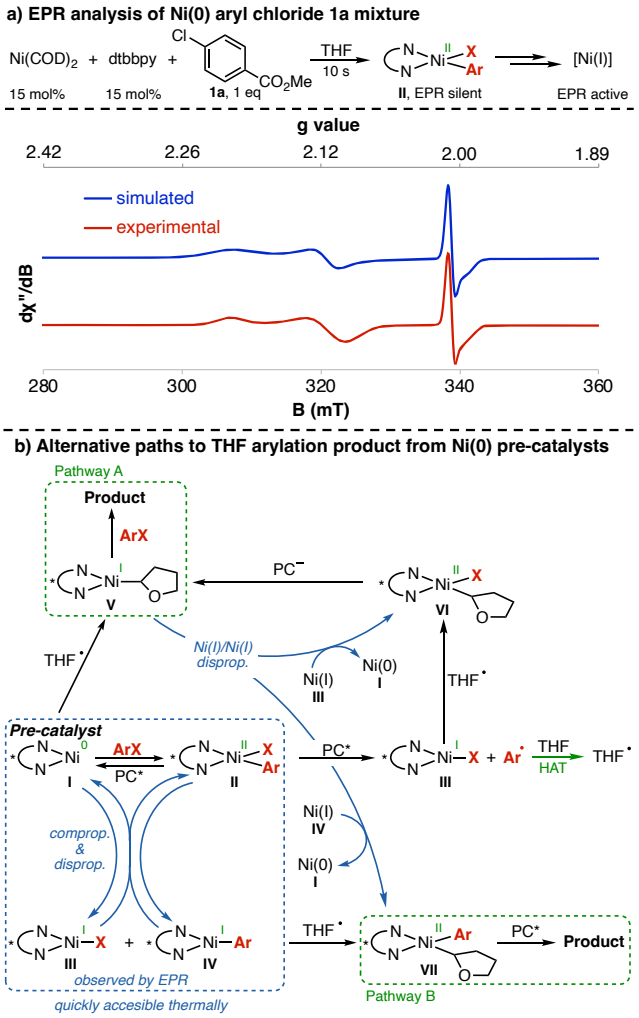

EPR reaction conditions: $Ni(COD)_2$ (0.0125 mmol), dtbbpy (0.0125 mmol), aryl chloride **1a** (0.125 mmol) and 0.5 mL of THF, frozen after 10 s. Temperature = 77 K, solvent = THF, microwave frequency = 9.501 GHz, microwave power = 2 mW, modulation amplitude = 8.0 G, modulation frequency = 1 mT/100 kHz. The simulation was performed using Simultispin[19] for Easyspin in MATLAB. The simulated spectrum uses the following parameters: g = [1.989, 2.004, 2.005], g = [1.885, 2.114, 2.208].

These mixing experiments demonstrate that four different Ni complexes (**I**-**IV**) are readily accessed solely by thermal pathways when mixing Ni(0), dtbbpy, and aryl chlorides or bromides. Additionally, it should be noted that for reactions starting from oxidative addition intermediate **II,** Ni(0) complex **I** and Ni(I) complex **III** have also been shown to be accessible under photochemical conditions.[2f-h, 5] Thus, multiple pathways to these intermediates can be envisioned.

Figure 6b details each of the possible pathways to THF arylation product that would arise from the trapping of the THF radical by different Ni species detected, or likely to be present, in solution at early time points. The product generation that originates from the THF radical trapping by **II**, the dominant pathway at later timepoints or when starting from $NiCl_2$, is not featured in this figure for simplicity.

Pathways A and B were envisioned as possible product formation manifolds that are relevant to consider at early time points (Figure 6b). Pathway A involves radical trapping by Ni(0) complex **I**, followed by subsequent oxidative addition of ArX and reductive elimination to generate product. This pathway is reminiscent of the mechanism proposed by the Kozlowski and Molander groups in the enantioselective arylation of benzylic trifluoroborate salts under Ni-photoredox conditions utilizing aryl bromides.[18] Pathway B involves reductive elimination from Ni(II) complex **VII**, which Doyle has recently proposed to be a photochemically induced step.[5, 15b, 20] Intermediate **VII** can potentially be accessed via two different routes: (1) THF radical trapping by Ni aryl complex **IV** (which was implicated by EPR), or (2) disproportionation of **V** and **IV** (blue arrows, Figure 6b). Finally, the THF radical could be trapped by Ni(I) halide **III**, also implicated as present in solution by the EPR studies, to render Ni(II) intermediate **VI**. This intermediate can also be accessed by the addition of the THF radical to the Ni(II) dihalide. The resulting Ni(III) THF dihalide complex could subsequently either undergo reductive elimination to yield halogenated THF (not detected) or intermediate **VI** via comproportionation with a Ni(I) complex. However, the only pathways to product from **VI** require additional steps that funnel back through either Pathway A or B.

To achieve product formation via Pathway A, oxidative addition of **V** into the aryl halide would have to outcompete disproportionation (with either Ni(I) species **III** or **IV**, Figure 6b). Based on prior Ni(I) oxidative addition rate studies, which show more sluggish reactivity for aryl chlorides,[1d, 1g, 2e, 21] Pathway A will be less favorable for aryl chlorides than aryl bromides. Notably, unlike Pathway A, Pathway B does not directly involve any intermediate containing a halide. Therefore, the simplest possible explanation for the observed matching e.r. at the initial time point (~68:32 e.r., Figure 5) is that Pathway B is dominant for product generation for both aryl chloride and bromide substrates at early time points.

So far, this paper has focused on the analysis of the Ni species that may be involved in the radical trapping event, whereas the THF radical generation mechanism has not been discussed. Our main assumption during these studies is that the radical generation and trapping events may be studied separately, which would not hold true if an in-cage formation and fast trapping of the THF radical were the main pathway. To challenge this hypothesis, which was initially proposed in the seminal report by Doyle,[3a] the Doyle lab recently conducted stoichiometric experiments that showcase the low efficiency of such a pathway.[5] Therefore our assumption is valid, and we can

move on from radical trapping to identifying relevant Ni species involved in THF radical formation.

The photolysis of the different reaction intermediates that are generated under these conditions has been extensively studied.[2b, 2f-h, 5, 8, 22] Given the low concentration in solution of the excited photocatalyst, it is most likely that the photoinduced radical generation step will preferentially involve a Ni intermediate that is present in high concentration in solution. In line with this, most reports have focused on understanding the photolysis of different Ni(II) intermediates, which are the resting states for most Ni-photoredox reactions. We are not implying that other photolysis pathways involving Ni complexes in other oxidation states are not at all viable, but the lower likelihood of those events would render those pathways minor. Finally, in agreement with the reported stoichiometric studies by the Hadt and Doyle groups,[2b, 2f-h, 5] an energy transfer process to a Ni(II) intermediate is most likely.[22] This is consistent with the reactivity we observed without photocatalyst for the aryl bromide reaction when a higher energy wavelength was employed (Table 1, entry 6).

Under our reaction conditions, three Ni(II) complexes may be predominant and undergo energy transfer with the photocatalyst:

(1) Complex **VII**, which would render the final product upon energy transfer (as previously mentioned, this is believed to be the pathway favored at high Ni(0) loading).

(2) Complex **II**, which has been shown to cleave the aryl moiety, not the halogen ligand, when excited.[2b, 2f-h, 5] Considering the solvent concentration of THF in our reaction, a fast HAT process to generate the THF radical and the reduced arene would be expected. If this were the main THF radical-formation pathway, considering that the aryl halide is the limiting reagent, a maximum yield of 50% would be obtained. This is not the case and the reduced arene is not a major byproduct, although it is observed in higher amounts when starting from Ni(0) pre-catalysts. For the model reaction utilizing **1a**, 6% yield of the reduced arene was measured by ^{1}H NMR when (BOX)Ni(COD) was used and no reduced arene was detected when starting from $NiCl_2$·glyme. This suggests that the photolysis of **II** leading to the THF radical generation pathway becomes more relevant when using a Ni(0) pre-catalyst. Another byproduct observed only when (BOX)Ni(COD) was used is the homo-coupled biaryl, which is also known to be generated at high concentrations of **II** via transmetallation (11% is obtained under these conditions, contrasting again with none being observed when $NiCl_2$·glyme is used). These results are not surprising considering the faster formation of **II** under the (BOX)Ni(COD) reaction conditions (see Figure 6b).

(3) Finally, the Ni(II) dihalide is both the starting pre-catalyst and a stable intermediate that has been shown to be the resting state of multiple Ni-photoredox systems.[1d, 1g] Because of the ubiquity of these intermediates, the study of their photolysis is very well-documented and has been shown to be accessible via energy transfer using Ir[dF(CF$_3$)ppy]$_2$(dtbbpy)PF$_6$.[2b, 2f-h, 5, 8, 22]

With all this information in hand, the proposed mechanism is depicted in Figure 7. Starting from the Ni(II) pre-catalyst **VIII**, an energy transfer from the excited photocatalyst will yield the halogen radical that facilitates the C–H cleavage to generate the α-oxygen THF radical.[22] This photolysis will also render Ni(I) halide (**III**), which can undergo oxidative addition into the aryl halide (**1**) to yield the highly reactive Ni(III) complex **IX**. A direct photolysis of **IX** to yield Ni(II) intermediate **II** could be envisioned. However, although this may be thermodynamically feasible,[3b] the reduced photon availability together with the fast kinetics of disproportionation in the presence of Ni(I) complexes makes the latter (**III** + **IX** → **II** + **VIII**) a more likely pathway.[2b-e] At this stage, the THF radical generation cycle can resume and Ni(II) intermediate **II** has been formed. The stoichiometric experiments detailed in Table 2, along with the unifying MLR model that captures the catalyst features driving enantioinduction for both aryl bromides and chlorides together (Figure 2b), both support complex **II** is involved in the dominant THF radical trapping event.[14] These experiments highlighted how the divergence in enantioselectivity observed when changing the halide (Figure 2a) can be explained by the different properties of **II** bearing either a chloride or a bromide. This radical trapping event leads to the formation of intermediate **X**, which is poised to readily undergo reductive elimination and yield arylated product **2**.

Additionally, this mechanism is also consistent with the initially higher enantioselectivity observed when using $NiCl_2$·glyme as the pre-catalyst with aryl bromide substrates. During the initial turnovers, the $NiCl_2$ pre-catalyst is expected to first bind to the BOX ligand and to form **VIII**, where both halogens would be chlorides. Photolysis of this intermediate yields **III** (X = Cl), which, after oxidative

Figure 7. Proposed mechanistic dependence on Ni pre-catalyst and time

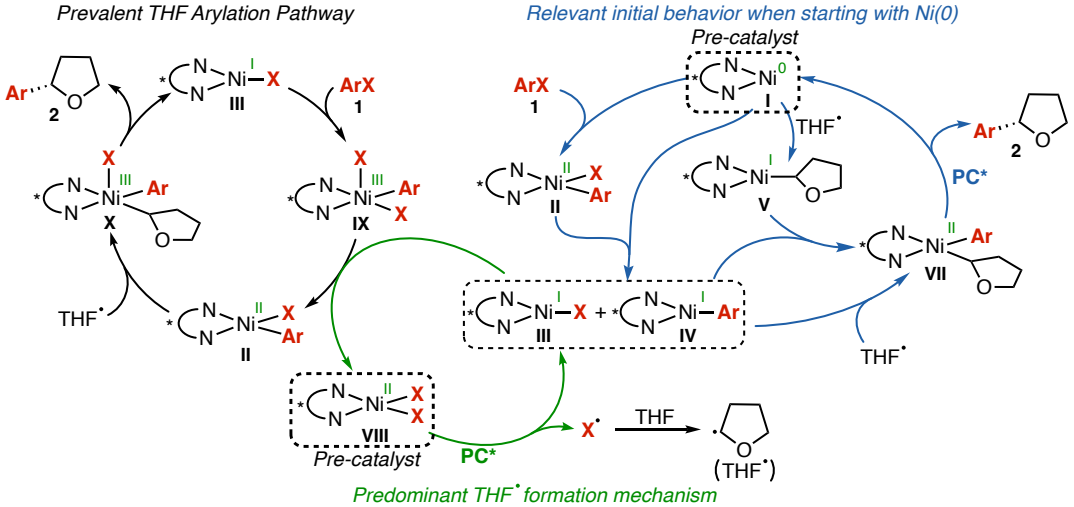

addition and disproportionation, would lead to the formation of Ni(II) intermediate **II** as a mixture of (BOX)Ni(Ar)(Cl) and (BOX)Ni(Ar)(Br). The presence of the (BOX)Ni(Ar)(Cl) would lead to product formation with higher enantioselectivity than that formed from the bromide adduct (Table 2). As the reaction proceeds, the ratio of bromide to chloride ions will quickly increase and the reactivity becomes dominated by the (BOX)Ni(Ar)(Br) complex and the accompanying lower levels of enantioenrichment observed (Table 2, entries 1 and 2). Indeed, when eliminating the complexity of competing halides by initiating the aryl bromide reaction using $NiBr_2$·glyme, we observed the expected lower e.r. throughout the reaction (Figure 5, red circles).

It is proposed that this is the dominant pathway when starting from $NiCl_2$·glyme and that also becomes prevalent after a short period when starting from (BOX)Ni(COD). The pervasiveness of this pathway is thought to be related to the higher stability of **II** and **VIII**. Additionally, these intermediates can be accessed via multiple disproportionation and comproportionation pathways,[2a-e] and thus are likely to be the Ni resting states during the reaction, from which radical trapping and generation can most readily occur. This dominant pathway is consistent with the mechanistic investigation recently reported by the Doyle lab, which proposes the black and green catalytic cycles (Figure 7) based on a different set of experiments that does not include an enantioselectivity readout.[5] No alternative pathways depending on the Ni source, or evolution of the mechanism over time, are proposed in that report.

However, our enantioselectivity data from the crossover experiments highlighted a discrepancy in the mechanism when starting from Ni(II) complex **II** (Figure 4). A dependence of enantiocontrol on the Ni source was again observed when utilizing (BOX)Ni(COD) as the pre-catalyst (Table 3), which showed a modest effect that was magnified when analyzing the product enantioselectivity at early time points (Figure 5). Leveraging EPR analysis showing **III** and **IV** to be thermally accessible when mixing Ni(0) and aryl halides **1a** or **1b** (Figure 6a), two feasible pathways were identified to account for this behavior (Figure 7, blue cycle). The direct trapping of the THF radical by Ni(0) **I**[18] yields Ni(I) complex **V**, which is prone to disproportionation (blue arrows, Figure 6b). Concurrently, the trapping of the THF radical by **IV** may also be involved in the formation of **VII**. At this stage, direct reductive elimination is likely slow, but can be accelerated by energy transfer from the excited photocatalyst. [5, 15b, 20, 22]

CONCLUSION

In summary, the development of an asymmetric variant of the Ni-photoredox THF arylation is described. Intriguing discrepancies in the product enantioselectivity were observed when switching from aryl chlorides to bromides and when changing the Ni pre-catalyst from $NiCl_2$·glyme to (BOX)Ni(COD). To explain this unexpected behavior, this paper presents a series of stoichiometric experiments, time course analyses of product enantioselectivity, EPR analysis of different reaction component mixtures, and a unifying MLR model correlating enantioselectivity with the properties of a key Ni intermediate. These experiments highlighted the presence of a dominant mechanism, where Ni(II) aryl halide complex **II** traps the THF radical and leads to product formation. This dominant mechanism is operative from the outset when using $NiCl_2$·glyme, and also becomes prevalent after a short period of time when using (BOX)Ni(COD) as the pre-catalyst.

Notably, a different manifold observed in the initial reaction stages when using (BOX)Ni(COD) is uncovered, thereby highlighting the potential for subtle mechanistic inquiries using the approach described in this paper. Thus, this work showcases a complex mechanistic landscape for the asymmetric THF arylation reaction that is common for aryl chlorides and bromides but diverges when changing the Ni pre-catalyst. It is believed that this intricate mechanistic picture is not unique to this Ni-photoredox reaction and that the approach utilized in this paper will help inform the study of other related systems.

ASSOCIATED CONTENT

Supporting Information

The supporting information is available free of charge on…
Experimental procedures, experimental and computational data, and characterization and spectral data for new compounds.
CCDC deposition number of **II-Br2**: 2360934.

AUTHOR INFORMATION

Corresponding Author

*ana.bahamonde@ucr.edu

Author Contributions

The manuscript was written through contributions of all authors.

ACKNOWLEDGMENT

The authors thank Veronica Carta and Phillip Farias for their assistance with the X-Ray measurements. This work was supported by the NSF (CHE-2235778), ACCESS (CHE220004), and the University of California, Riverside.

REFERENCES

1. (a) Tasker, S. Z.; Standley, E. A.; Jamison, T. F., Recent advances in homogeneous nickel catalysis. *Nature* **2014,** *509*, 299-309; (b) Vila, C., Merging Visible-Light-Photoredox and Nickel Catalysis. *Chem. Cat. Chem.* **2015,** *7*, 1790-1793; (c) Wang, C.-S.; Dixneuf, P. H.; Soulé, J.-F., Photoredox Catalysis for Building C–C Bonds from C(sp2)–H Bonds. *Chem. Rev.* **2018,** *118*, 7532-7585; (d) Diccianni, J. B.; Diao, T., Mechanisms of nickel-catalyzed cross-coupling reactions. *Trends in Chemistry* **2019,** *1*, 830-844; (e) Zhu, C.; Yue, H.; Jia, J.; Rueping, M., Recent Advances in Nickel-Catalyzed C-Heteroatom Cross-Coupling Reactions under Mild Conditions via Facilitated Reductive Elimination. *Angew. Chem.* **2020,** *60*, 17810-17831; (f) Chan, A. Y.; Perry, I. B.; Bissonnette, N. B.; Buksh, B. F.; Edwards, G. A.; Frye, L. I.; Garry, O. L.; Lavagnino, M. N.; Li, B. X.; Liang, Y.; Mao, E.; Millet, A.; Oakley, J. V.; Reed, N. L.; Sakai, H. A.; Seath, C. P.; MacMillan, D. W. C., Metallaphotoredox: The Merger of Photoredox and Transition Metal Catalysis. *Chem. Rev.* **2022,** *122*, 1485-1542; (g) Cagan, D. A.; Bím, D.; Kazmierczak, N. P.; Hadt, R. G., Mechanisms of Photoredox Catalysis Featuring Nickel–Bipyridine Complexes. *ACS Catal.* **2024,** *14*, 9055-9076.

2. (a) Bradley, R. D.; McManus, B. D.; Yam, J. G.; Carta, V.; Bahamonde, A., Mechanistic Evidence of a Ni (0/II/III) Cycle for Nickel Photoredox Amide Arylation. *Angew. Chem. Int. Ed.* **2023,** *62*, e202310753; (b) Cagan, D. A.; Bím, D.; McNicholas, B. J.; Kazmierczak, N. P.; Oyala, P. H.; Hadt, R. G., Photogenerated Ni (I)–Bipyridine Halide Complexes: Structure–Function Relationships for

Competitive C (sp2)–Cl Oxidative Addition and Dimerization Reactivity Pathways. *Inorg Chem* **2023,** *62*, 9538-9551; (c) Kawamata, Y.; Vantourout, J. C.; Hickey, D. P.; Bai, P.; Chen, L.; Hou, Q.; Qiao, W.; Barman, K.; Edwards, M. A.; Garrido-Castro, A. F., Electrochemically driven, Ni-catalyzed aryl amination: scope, mechanism, and applications. *J. Am. Chem. Soc.* **2019,** *141*, 6392-6402; (d) Newman-Stonebraker, S. H.; Raab, T. J.; Roshandel, H.; Doyle, A. G., Synthesis of Nickel (I)–Bromide Complexes via Oxidation and Ligand Displacement: Evaluation of Ligand Effects on Speciation and Reactivity. *J. Am. Chem. Soc.* **2023,** *145*, 19368-19377; (e) Ting, S. I.; Williams, W. L.; Doyle, A. G., Oxidative addition of aryl halides to a Ni (I)-bipyridine complex. *J. Am. Chem. Soc.* **2022,** *144*, 5575-5582; (f) Cagan, D. A.; Stroscio, G. D.; Cusumano, A. Q.; Hadt, R. G., Multireference description of nickel–aryl homolytic bond dissociation processes in photoredox catalysis. *The Journal of Physical Chemistry A* **2020,** *124*, 9915-9922; (g) Cagan, D. A.; Bím, D.; Silva, B.; Kazmierczak, N. P.; McNicholas, B. J.; Hadt, R. G., Elucidating the mechanism of excited-state bond homolysis in nickel–bipyridine photoredox catalysts. *J. Am. Chem. Soc.* **2022,** *144*, 6516-6531; (h) Ting, S. I.; Garakyaraghi, S.; Taliaferro, C. M.; Shields, B. J.; Scholes, G. D.; Castellano, F. N.; Doyle, A. G., 3d-d excited states of Ni (II) complexes relevant to photoredox catalysis: Spectroscopic identification and mechanistic implications. *J. Am. Chem. Soc.* **2020,** *142*, 5800-5810.

3. (a) Shields, B. J.; Doyle, A. G., Direct C(sp3)–H Cross Coupling Enabled by Catalytic Generation of Chlorine Radicals. *J. Am. Chem. Soc.* **2016,** *138*, 12719-12722; (b) Heitz, D. R.; Tellis, J. C.; Molander, G. A., Photochemical nickel-catalyzed C–H arylation: synthetic scope and mechanistic investigations. *J. Am. Chem. Soc.* **2016,** *138*, 12715-12718; (c) Ackerman, L. K.; Martinez Alvarado, J. I.; Doyle, A. G., Direct C–C bond formation from alkanes using Ni-photoredox catalysis. *J. Am. Chem. Soc.* **2018,** *140*, 14059-14063; (d) Cheng, X.; Lu, H.; Lu, Z., Enantioselective benzylic C–H arylation via photoredox and nickel dual catalysis. *Nat. Comm.* **2019,** *10*, 3549; (e) Deng, H.-P.; Fan, X.-Z.; Chen, Z.-H.; Xu, Q.-H.; Wu, J., Photoinduced nickel-catalyzed chemo-and regioselective hydroalkylation of internal alkynes with ether and amide α-hetero C (sp3)–H bonds. *J. Am. Chem. Soc.* **2017,** *139*, 13579-13584; (f) Huan, L.; Shu, X.; Zu, W.; Zhong, D.; Huo, H., Asymmetric benzylic C (sp3)– H acylation via dual nickel and photoredox catalysis. *Nat. Comm.* **2021,** *12*, 3536; (g) Huang, L.; Rueping, M., Direct Cross-Coupling of Allylic C (sp3)– H Bonds with Aryl-and Vinylbromides by Combined Nickel and Visible-Light Catalysis. *Angew. Chem.* **2018,** *130*, 10490-10494; (h) Kariofillis, S. K.; Doyle, A. G., Synthetic and Mechanistic Implications of Chlorine Photoelimination in Nickel/Photoredox C (sp3)–H Cross-Coupling. *Acc. Chem. Res.* **2021,** *54*, 988-1000; (i) Nielsen, M. K.; Shields, B. J.; Liu, J.; Williams, M. J.; Zacuto, M. J.; Doyle, A. G., Mild, redox-neutral formylation of aryl chlorides through the photocatalytic generation of chlorine radicals. *Angew. Chem. Int. Ed.* **2017,** *56*, 7191-7194; (j) Rand, A. W.; Yin, H.; Xu, L.; Giacoboni, J.; Martin-Montero, R.; Romano, C.; Montgomery, J.; Martin, R., Dual catalytic platform for enabling sp3 α C–H arylation and alkylation of benzamides. *ACS Catal.* **2020,** *10*, 4671-4676; (k) Santos, M. S.; Corrêa, A. G.; Paixão, M. W.; König, B., C (sp3)– C (sp3) Cross-Coupling of Alkyl Bromides and Ethers Mediated by Metal and Visible Light Photoredox Catalysis. *Adv. Synth. Catal.* **2020,** *362*, 2367-2372; (l) Shu, X.; Huan, L.; Huang, Q.; Huo, H., Direct enantioselective C (sp3)–H acylation for the synthesis of α-amino ketones. *J. Am. Chem. Soc.* **2020,** *142*, 19058-19064; (m) Shu, X.; Zhong, D.; Lin, Y.; Qin, X.; Huo, H., Modular access to chiral α-(hetero) aryl amines via Ni/photoredox-catalyzed enantioselective cross-coupling. *J. Am. Chem. Soc.* **2022,** *144*, 8797-8806; (n) Sun, Z.; Kumagai, N.; Shibasaki, M., Photocatalytic α-acylation of ethers. *Org. Lett.* **2017,** *19*, 3727-3730.

4. For another Ni-photoredox enantioselective THF arylation using a different mechanistic manifold see: Xu, S.; Ping, Y.; Li, W.; Guo, H.; Su, Y.; Li, Z.; Wang, M.; Kong, W., Enantioselective C (sp3)–H functionalization of oxacycles via photo-HAT/nickel dual catalysis. J. Am. Chem. Soc. 2023, 145, 5231-5241.

5. Cusumano, A. Q.; Chaffin, B. C.; Doyle, A. G., Mechanism of Ni-Catalyzed Photochemical Halogen Atom-Mediated C (sp3)–H Arylation. *J. Am. Chem. Soc.* **2024,** *146*, 15331-15344.

6. (a) Yin, H.; Fu, G. C., Mechanistic Investigation of Enantioconvergent Kumada Reactions of Racemic α-Bromoketones Catalyzed by a Nickel/Bis(oxazoline) Complex. *J. Am. Chem. Soc.* **2019,** *141*, 15433-15440; (b) Turro, R. F.; Wahlman, J. L. H.; Tong, Z. J.; Chen, X.; Yang, M.; Chen, E. P.; Hong, X.; Hadt, R. G.; Houk, K. N.; Yang, Y.-F.; Reisman, S. E., Mechanistic Investigation of Ni-Catalyzed Reductive Cross-Coupling of Alkenyl and Benzyl Electrophiles. *J. Am. Chem. Soc.* **2023,** *145*, 14705-14715; (c) McNicholas, B. J.; Tong, Z. J.; Bím, D.; Turro, R. F.; Kazmierczak, N. P.; Chalupský, J.; Reisman, S. E.; Hadt, R. G., Electronic Structures of Nickel(II)-Bis(indanyloxazoline)-dihalide Catalysts: Understanding Ligand Field Contributions That Promote C(sp2)–C(sp3) Cross-Coupling. *Inorg Chem* **2023,** *62*, 14010-14027.

7. (a) Lau, S. H.; Borden, M.; Steiman, T.; Wang, L.; Parasram, M.; Doyle, A., Ni/Photoredox-Catalyzed Enantioselective Cross-Electrophile Coupling of Styrene Oxides with Aryl Iodides. *J. Am. Chem. Soc.* **2021,** *143*, 15873–15881; (b) Santiago, C. B.; Guo, J.-Y.; Sigman, M. S., Predictive and mechanistic multivariate linear regression models for reaction development. *Chem. Sci.* **2018,** *9*, 2398-2412; (c) Sigman, M. S.; Harper, K. C.; Bess, E. N.; Milo, A., The development of multidimensional analysis tools for asymmetric catalysis and beyond. *Acc. Chem. Res.* **2016,** *49*, 1292-1301; (d) Akana, M. E.; Tcyrulnikov, S.; Akana-Schneider, B. D.; Reyes, G. P.; Monfette, S.; Sigman, M. S.; Hansen, E. C.; Weix, D. J., Computational Methods Enable the Prediction of Improved Catalysts for Nickel-Catalyzed Cross-Electrophile Coupling. *J. Am. Chem. Soc.* **2024,** *146*, 3043-3051.

8. (a) Li, G.; Yang, L.; Liu, J. J.; Zhang, W.; Cao, R.; Wang, C.; Zhang, Z.; Xiao, J.; Xue, D., Light-Promoted C–N Coupling of Aryl Halides with Nitroarenes. *Angew. Chem. Int. Ed.* **2021,** *60*, 5230-5234; (b) Song, G.; Yang, L.; Li, J. S.; Tang, W. J.; Zhang, W.; Cao, R.; Wang, C.; Xiao, J.; Xue, D., Chiral arylated amines via C– N coupling of chiral amines with aryl bromides promoted by light. *Angew. Chem. Int. Ed.* **2021,** *60*, 21536-21542; (c) Song, G.; Li, Q.; Nong, D.-Z.; Song, J.; Li, G.; Wang, C.; Xiao, J.; Xue, D., Ni-Catalyzed Photochemical C–N Coupling of Amides with (Hetero)aryl Chlorides. *Eur. J. Chem.* **2023,** *29*, e202300458.

9. (a) Lu, C.; Wu, C.; Ghoreishi, D.; Chen, W.; Wang, L.; Damm, W.; Ross, G. A.; Dahlgren, M. K.; Russell, E.; Von Bargen, C. D.; Abel, R.; Friesner, R. A.; Harder, E. D., OPLS4: Improving Force Field Accuracy on Challenging Regimes of Chemical Space. *Journal of Chemical Theory and Computation* **2021,** *17*, 4291-4300; (b) Roos, K.; Wu, C.; Damm, W.; Reboul, M.; Stevenson, J. M.; Lu, C.; Dahlgren, M. K.; Mondal, S.; Chen, W.; Wang, L.; Abel, R.; Friesner, R. A.; Harder, E. D., OPLS3e: Extending Force Field Coverage for Drug-Like Small Molecules. *Journal of Chemical Theory and Computation* **2019,** *15*, 1863-1874.

10. (a) *MacroModel*, version 2024-2, Schrödinger, LLC: New York, NY 2024. (b) Watts, K. S.; Dalal, P.; Tebben, A. J.; Cheney, D. L.; Shelley, J. C., Macrocycle Conformational Sampling with MacroModel. *Journal of Chemical Information and Modeling* **2014,** *54*, 2680-2696; (c) Mohamadi, F.; Richards, N. G.; Guida, W. C.; Liskamp, R.; Lipton, M.; Caufield, C.; Chang, G.; Hendrickson, T.; Still, W. C., Macromodel—an integrated software system for modeling organic and bioorganic molecules using molecular mechanics. *Journal of Computational Chemistry* **1990,** *11*, 440-467.

11. (a) Becke, A., Density-functional thermochemistry. III. The role of exact exchange. *J. Chem. Phys.* **1993,** *98*, 5648; (b) Clark, T.; Chandrasekhar, J.; Spitznagel, G. W.; Schleyer, P. V. R., Efficient diffuse function-augmented basis sets for anion calculations. III. The 3-21+ G basis set for first-row elements, Li–F. *Journal of Computational Chemistry*

1983, *4*, 294-301; (c) Francl, M. M.; Pietro, W. J.; Hehre, W. J.; Binkley, J. S.; Gordon, M. S.; DeFrees, D. J.; Pople, J. A., Self-consistent molecular orbital methods. XXIII. A polarization-type basis set for second-row elements. *The Journal of Chemical Physics* **1982,** *77*, 3654-3665; (d) Grimme, S.; Antony, J.; Ehrlich, S.; Krieg, H., A consistent and accurate ab initio parametrization of density functional dispersion correction (DFT-D) for the 94 elements H-Pu. *The Journal of chemical physics* **2010,** *132*, 154104; (e) Grimme, S.; Ehrlich, S.; Goerigk, L., Effect of the damping function in dispersion corrected density functional theory. *Journal of computational chemistry* **2011,** *32*, 1456-1465; (f) Johnson, E. R.; Becke, A. D., A post-Hartree–Fock model of intermolecular interactions. *The Journal of chemical physics* **2005,** *123*, 024101; (g) Johnson, E. R.; Becke, A. D., A post-Hartree-Fock model of intermolecular interactions: Inclusion of higher-order corrections. *The Journal of chemical physics* **2006,** *124*, 174104; (h) Krishnan, R.; Binkley, J. S.; Seeger, R.; Pople, J. A., Self-consistent molecular orbital methods. XX. A basis set for correlated wave functions. *The Journal of chemical physics* **1980,** *72*, 650-654; (i) Marenich, A. V.; Cramer, C. J.; Truhlar, D. G., Universal solvation model based on solute electron density and on a continuum model of the solvent defined by the bulk dielectric constant and atomic surface tensions. *The Journal of Physical Chemistry B* **2009,** *113*, 6378-6396; (j) McLean, A.; Chandler, G., Contracted Gaussian basis sets for molecular calculations. I. Second row atoms, Z= 11–18. *The Journal of chemical physics* **1980,** *72*, 5639-5648; (k) Spitznagel, G. W.; Clark, T.; von Ragué Schleyer, P.; Hehre, W. J., An evaluation of the performance of diffuse function-augmented basis sets for second row elements, Na-Cl. *Journal of computational chemistry* **1987,** *8*, 1109-1116; (l) Towns, J.; Cockerill, T.; Dahan, M.; Foster, I.; Gaither, K.; Grimshaw, A.; Hazlewood, V.; Lathrop, S.; Lifka, D.; Peterson, G. D., XSEDE: accelerating scientific discovery. *Computing in science & engineering* **2014,** *16*, 62-74; (m) Zhao, Y.; Truhlar, D. G., The M06 suite of density functionals for main group thermochemistry, thermochemical kinetics, noncovalent interactions, excited states, and transition elements: two new functionals and systematic testing of four M06-class functionals and 12 other functionals. *Theoretical chemistry accounts* **2008,** *120*, 215-241; (n) Andrae, D.; Haeussermann, U.; Dolg, M.; Stoll, H.; Preuss, H., Energy-adjusted ab initio pseudopotentials for the second and third row transition elements. *Theoretica chimica acta* **1990,** *77*, 123-141; (o) Hay, P. J.; Wadt, W. R., Ab initio effective core potentials for molecular calculations. Potentials for the transition metal atoms Sc to Hg. *The Journal of chemical physics* **1985,** *82*, 270-283; (p) Hay, P. J.; Wadt, W. R., Ab initio effective core potentials for molecular calculations. Potentials for K to Au including the outermost core orbitals. *The Journal of chemical physics* **1985,** *82*, 299-310; (q) Weigend, F.; Ahlrichs, R., Balanced basis sets of split valence, triple zeta valence and quadruple zeta valence quality for H to Rn: Design and assessment of accuracy. *Phys. Chem. Chem. Phys.* **2005,** *7*, 3297-3305.

12. Kennard, R. W.; Stone, L. A., Computer aided design of experiments. *Technometrics* **1969,** *11*, 137-148.

13. (a) Gransbury, G. K.; Corner, S. C.; Kragskow, J. G. C.; Evans, P.; Yeung, H. M.; Blackmore, W. J. A.; Whitehead, G. F. S.; Vitorica-Yrezabal, I. J.; Oakley, M. S.; Chilton, N. F.; Mills, D. P., AtomAccess: A Predictive Tool for Molecular Design and Its Application to the Targeted Synthesis of Dysprosium Single-Molecule Magnets. *J. Am. Chem. Soc.* **2023,** *145*, 22814-22825; (b) Gransbury, G. K. K., J. G. C.; Chilton, N. F Magnetism Tools: Atom Access. https://magnetism-tools.manchester.ac.uk/apps/atom_access_app (accessed 2024-05-15).

14. Lin, Q.; Spielvogel, E. H.; Diao, T., Carbon-centered radical capture at nickel (II) complexes: Spectroscopic evidence, rates, and selectivity. *Chem* **2023,** *9*, 1295-1308.

15. (a) Ju, L.; Lin, Q.; LiBretto, N. J.; Wagner, C. L.; Hu, C. T.; Miller, J. T.; Diao, T., Reactivity of (bi-Oxazoline)organonickel Complexes and Revision of a Catalytic Mechanism. *J. Am. Chem. Soc.* **2021,** *143*, 14458-14463; (b) Ju, L.; Hu, C. T.; Diao, T., Strategies for Promoting Reductive Elimination of Bi-and Bis-Oxazoline Ligated Organonickel Complexes. *Organometallics* **2022,** *41*, 1748-1753; (c) Dawson, G. A.; Lin, Q.; Neary, M. C.; Diao, T., Ligand Redox Activity of Organonickel Radical Complexes Governed by the Geometry. *J. Am. Chem. Soc.* **2023,** *145*, 20551-20561.

16. (a) Wang, Z.; Yin, H.; Fu, G. C., Catalytic enantioconvergent coupling of secondary and tertiary electrophiles with olefins. *Nature* **2018,** *563*, 379-383; (b) Tong, X.; Schneck, F.; Fu, G. C., Catalytic Enantioselective α-Alkylation of Amides by Unactivated Alkyl Electrophiles. *J. Am. Chem. Soc.* **2022,** *144*, 14856-14863.

17. Gong, Y.; Su, L.; Zhu, Z.; Ye, Y.; Gong, H., Nickel-Catalyzed Thermal Redox Functionalization of C (sp3)– H Bonds with Carbon Electrophiles. *Angew. Chem. Int. Ed.* **2022,** *61*, e202201662.

18. Gutierrez, O.; Tellis, J. C.; Primer, D. N.; Molander, G. A.; Kozlowski, M. C., Nickel-catalyzed cross-coupling of photoredox-generated radicals: uncovering a general manifold for stereoconvergence in nickel-catalyzed cross-couplings. *J. Am. Chem. Soc.* **2015,** *137*, 4896-4899.

19. Molton, F., Simultispin: A versatile graphical user interface for the simulation of solid-state continuous wave EPR spectra. *Magnetic Resonance in Chemistry* **2020,** *58*, 718-726.

20. (a) Komiya, S.; Abe, Y.; Yamamoto, A.; Yamamoto, T., Phosphine-induced reductive elimination from cis-arylmethylnickel (II) complexes having a 1, 2-bis (dimethylphosphino) ethane ligand. *Organometallics* **1983,** *2*, 1466-1468; (b) Welin, E. R.; Le, C.; Arias-Rotondo, D. M.; McCusker, J. K.; MacMillan, D. W., Photosensitized, energy transfer-mediated organometallic catalysis through electronically excited nickel (II). *Science* **2017,** *355*, 380-385.

21. Lin, Q.; Diao, T., Mechanism of Ni-catalyzed reductive 1, 2-dicarbofunctionalization of alkenes. *J. Am. Chem. Soc.* **2019,** *141*, 17937-17948.

22. DiLuzio, S.; Kannadi Valloli, L.; Kudisch, M.; Chambers, D. T.; Rumbles, G.; Reid, O. G.; Bird, M. J.; Sayre, H. J., Reconceptualizing the IrIII Role in Metallaphotoredox Catalysis: From Strong Photooxidant to Potent Energy Donor. *ACS Catal.* **2024,** *14*, 11378-11388.

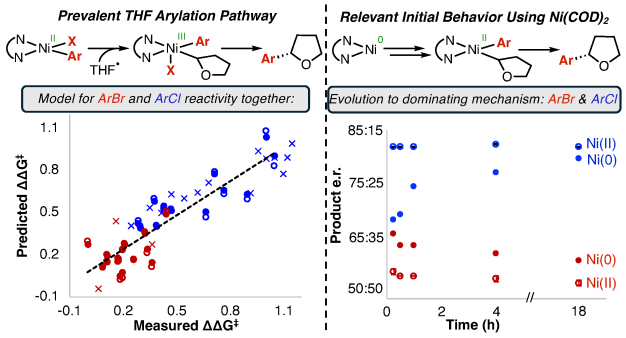
Prevalent THF Arylation Pathway
Relevant Initial Behavior Using Ni(COD)2
THF•
Model for ArBr and ArCl reactivity together:
Evolution to dominating mechanism: ArBr & ArCl
Predicted ΔΔG‡
Measured ΔΔG‡
1.1
0.8
0.5
0.2
-0.1
-0.1
0.2
0.5
0.8
1.1
Product e.r.
85:15
75:25
65:35
50:50
Time (h)
0
2
4
18
Ni(II)
Ni(0)
Ni(0)
Ni(II)